Biointerphases
a SpringerOpen Journal

ORIGINAL ARTICLE Open Access

# Cell membrane topology analysis by RICM enables marker-free adhesion strength quantification

Katharina Klein[1], Christina E Rommel[2], Vera C Hirschfeld-Warneken[1] and Joachim P Spatz[1*]

**Abstract**

Reflection interference contrast microscopy (RICM) allows the visualization of the cell's adhesion topology on substrates. Here it is applied as a new label-free method to measure adhesion forces between tumor cells and their substrate without any external manipulation, i.e., the application of force or adjustments in the substrate elasticity. Malignant cancer transformation is closely associated with the down-regulation of adhesion proteins and the consequent reduction of adhesion forces. By analyzing the size and distribution of adhesion patches from a benign and a malignant human pancreatic tumor cell line, we established a model for calculating the adhesion strength based on RICM images. Further, we could show that the cell's spread area does not necessarily scale with adhesion strength. Despite the larger projected cell area of the malignant cell line, adhesion strength was clearly reduced. This underscores the importance of adhesion patch analysis. The calculated force values were verified by microfluidic detachment assays. Static and dynamic RICM measurements produce numerous adhesion-related parameters from which characteristic cell signatures can be derived. Such a cellular fingerprint can refine the process of categorizing cell lines according to their grade of differentiation.

**Keywords:** RICM; Cell adhesion; Adhesion patches; Adhesion maps; Adhesion kinetics; Microfluidic cell detachment assay; Adhesion strength model

## Background

Cell adhesion is central to the development and organization as well as the maintenance and repair of tissue, because cell-matrix and cell-cell interactions provide anchoring and triggering of cell signaling processes related to survival, proliferation, differentiation, motility and, in particular, tumor cell transformation [1,2]. Cell adhesion is a time-dependent process: adhesive components develop within several hours after initial cell binding to the extracellular matrix (ECM); next adhesion strengthening occurs, at first through cell spreading, integrin aggregation and focal adhesion (FA) formation, and then via the generation of mechanical forces by the actin-myosin network [3].

Commonly used techniques for characterizing cell matrix adhesion include the analysis of cell spreading, migration and FA formation as well as simple wash assays. But all of these methods are merely indirect indicators of adhesion strength and do not provide a quantitative measurement of the forces and stresses involved in cell adhesion.

There exist two classes of quantitative force assays: 1. Traction force assays, which provide an indirect measurement of the adhesion strength. These require a suitable elastic substrate that displays particle displacement generated by an applied force. A limitation of this method is the fact that substrate elasticity directly impacts the force generation of cells [4,5]. 2. Detachment assays, which quantify the forces required to detach a cell from the substrate. Examples of detachment assays include centrifuge assays and several hydrodynamic shear assays as well as single cell micromanipulation techniques, such as atomic force microscopy [6].

* Correspondence: spatz@is.mpg.de
[1]Department of New Materials and Biosystems, Max Planck Institute for Intelligent Systems, Stuttgart, Germany, and Department of Biophysical Chemistry, University of Heidelberg, Heidelberg, Germany
Full list of author information is available at the end of the article

Abnormalities in adhesive interactions, caused by changes in the complex cell adhesion process, are often associated with pathological states such as tumor cell transformation [7]. Most tumors originate from the epithelial layer, where cell adhesion plays an important role. During tumor progression, changes in adhesion behavior occur. It is commonly assumed that in most cases epithelial-derived tumor cells undergo an epithelial to mesenchymal transition, accompanied by a down-regulation of adhesion-supporting proteins and a simultaneous up-regulation of migration-aiding proteins [8,9]. In carcinomas the loss of functional cell polarity and cell adhesion typically represent a requirement for the invasive and metastatic potential of the tumor cells [10].

Dysfunctions in adhesion and adhesion-related proteins in tumor cells induce subtle alterations in the adhesion pattern, a process that cannot be visualized by standard light microscopy in real-time. Reflection interference contrast microscopy (RICM), with its ability to measure inter-surface distances between a cell and a flat substrate in aqueous conditions with a nanometer precision of ~5 nm [11], has proven to be very useful in imaging adhesion zones in real-time and valuable information on the nature of adhesions can be derived from these data [12-16]. Since RICM image formation merely relies on the reflection of light at the different interphases (Figure 1A), fluorophore labeling of cells beforehand is not required. In this sense, RICM provides a marker-free characterization technology for cell adhesion. More precisely, dark zones in the RICM image correspond to close contact areas [17,18]. The interference pattern displays the exact adhesion topology and can serve to extract adhesion-related information. As a result, a characteristic adhesion-based fingerprint for a distinct cell type can be obtained. The resolution of RICM is actually so high, that small cell protrusions, which are rarely visible in bright field microscopy, can be made visible using this technique (Figure 1B).

In this study we used a pair of human sister cell lines, PaTu8988S (PatuS) and PaTu8988T (PatuT), which were derived from the same metastasis of a pancreas adenocarcinoma but differ in their grade of differentiation, i.e., their malignancy [19]. PatuT, in contrast to PatuS cells, do not express E-Cadherin receptors and therefore represent the malignant, dedifferentiated cell line. The loss in E-Cadherin expression is accompanied by enhanced migratory capabilities of PatuT cells (in comparison to PatuS cells), which were determined by an *in vitro* migration assay (so-called "scratch assay") [20]. A study where the two cell lines were implanted in the yolk sac

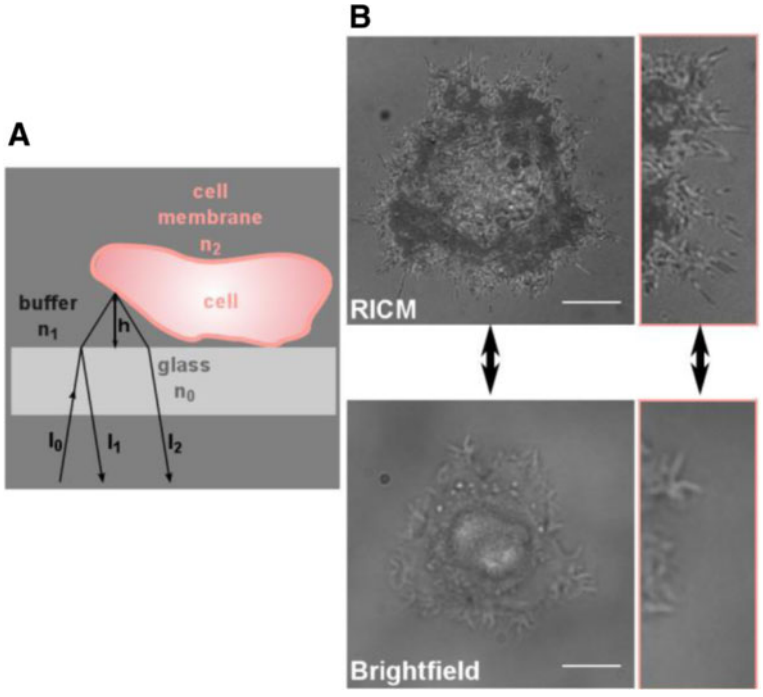


**Figure 1 Reflection interference contrast microscopy. (A)** Scheme depicting RICM image formation at the cell-surface interface. $I_1$ and $I_2$ are the intensities of the light reflected on the glass-buffer and the buffer-cell interface. The interference between these rays is measured. **(B)** RICM image (top) and brightfield image (bottom) of a cell. The RICM image displays different grey levels, which correspond to differences in the distance of the cell membrane to the glass interface. Darker areas represent close distances between the cell membrane and the glass interface, in other words, areas of cell adhesion. In addition, small cellular filopodia that are invisible in the brightfield image can be visualized with RICM (see image enlargements).

of a zebrafish embryo proved the more invasive and metastatic behavior of the PatuT cell line [20]. The PatuT cells also show a higher fractal dimension in their cell contour and adhesion topology that is correlated with a higher malignancy [16].

To better understand contact formation between the cell membrane and surface, especially in epithelial derived tumor cells with down-regulated adhesion properties, we monitored the individual cell adhesion kinetics of the two cancer cell lines PatuT and PatuS. Using RICM, we visualized adhesive contact formation between the cell membrane and the surface after contact initiation on collagen-coated glass surfaces. Based on the numerous data extracted from single adhesion map images and from the kinetic evolvement of individual parameters, we were able to differentiate between the two highly similar sister cell lines. The aim of this study was to prove the high potential of RICM images for visualizing subtle alterations in cell adhesion that occur during tumor progression and to use these data for the assignment of a tumor prognosis. By quantifying size and spatial arrangement of adhesion patches within a cell and implementing this data into a cell adhesion model, we were able to estimate the cell adhesion strength by a noninvasive optical method. The obtained results were verified with a microfluidic cell detachment assay, which involves exposing the cells to hydrodynamic shear stress.

RICM imaging is a powerful and well-established tool for cell adhesion analyses, as it provides non-invasive, marker-free, and real-time observation of living cells. In this study, we used a well-established method, the RICM technique, in a new context, namely adhesion strength calculation. By doing this, we took full advantage of RICM's unique benefit: the ability to provide detailed information about the cell contact area. This new take on a familiar method has the potential to be applied in a clinical setting for determining the metastatic potential of tumor cells.

## Methods

### Cell culture& immunocytochemistry

Two pancreatic tumor cell lines derived from the same metastasis of a pancreas tumor [19], Patu8988t (PatuT) and Patu8988s (PatuS), were obtained from the German collection of microorganisms and cell cultures (DSMZ). The cells were grown in DME (Dulbecco modified Eagle) medium supplemented with 5% FBS (fetal bovine serum; Life technologies) and 5% horse serum (Sigma) at 37°C and 5% $CO_2$. The culture medium was exchanged every 2 or 3 days. Cells were grown to 70-80% confluence and were then treated with 2.5% trypsin/EDTA (Gibco) and centrifuged (1200 rpm, 3 min). For RICM experiments $75\times10^3$ cells were cultured in 2 ml medium with 1% serum. For microfluidic experiments cells were stained with Cell Tracker Red or Cell Tracker Green® (Life technologies) within the culture flasks for 45 min prior to trypsinization and centrifugation. $5\times10^5$ cells of each stained cell line were mixed in 1 ml medium with 1% serum. Focal contacts were investigated 24 h after seeding by immunofluorescence staining of fixed PatuT cells using an antibody against paxillin (P13520, Transduction Laboratories; now: 610051, BD Biosciences), a known component of focal adhesions.

### Substrate coating

Glass coverslips (20×20 mm; Carl Roth) were cleaned in Piranha solution (hydrogen peroxide ($H_2O_2$) and concentrated sulfuric acid ($H_2SO_4$) at a ratio of 1:3) for 60 min, then rinsed with MilliQ® water and blown dry with nitrogen. Next, coverslips were incubated with collagen (collagen type I, rat tail, Harbor Bio-products) at a concentration of 100 μg/ml in 0.02 N acetic acid for 30 min at room temperature. After the coating step, the coverslips were rinsed with MilliQ® water and PBS buffer.

### Fabrication of microfluidic channels

Polydimethylsiloxane (PDMS, Sylgard 184; Dow Corning) single flow channels (25 mm × 3 mm × 40 μm) were produced by standard soft lithography techniques [21,22]. Briefly, the master (J.D. Phototools) was fabricated by photolithography based on the company´s protocol using a negative photo resist (SU-8 25; MicroChem Corporation) on a silicon wafer substrate (Si-Mat). The SU8 mold was coated with perfluorooctyltrichlorosilane (ABCR) prior to casting liquid PDMS. The PDMS template was cured for at least 4 hours at 65°C to fully crosslink the elastomer structure. Then, the PDMS block was peeled off the mask and was connected to tubes (PFTE, OD:1/16"; ID: .030"/75 mm; Vici®) through holes punched into the PDMS channel. The flow channel and a Piranha-cleaned coverslip (24×60 mm, Roth) were activated with oxygen plasma (30 s at 150 W, 0.5 mbar) and then connected to each other.

### Microfluidic cell detachment assay

Fluid flow was controlled by using a syringe pump system (Model AL-1000; World precision instrument) with 20 ml syringes (Braun). The channel consists of two inlets (one for the cell suspension, one for the cell culture media) and one outlet (Figure 2). A collagen solution (c = 100 μg/ml) was applied to coat the coverslip of the flow cell. After 30 min the flow chamber was rinsed with cell culture medium with 1% serum. Next, the cell suspension was pumped into the microfluidic channel and cells were allowed to adhere for 90 min. We chose a time span of 90 min to ensure that all cells were completely adhered to the substrate within the flow channel. Cells were visualized with the DeltaVision system

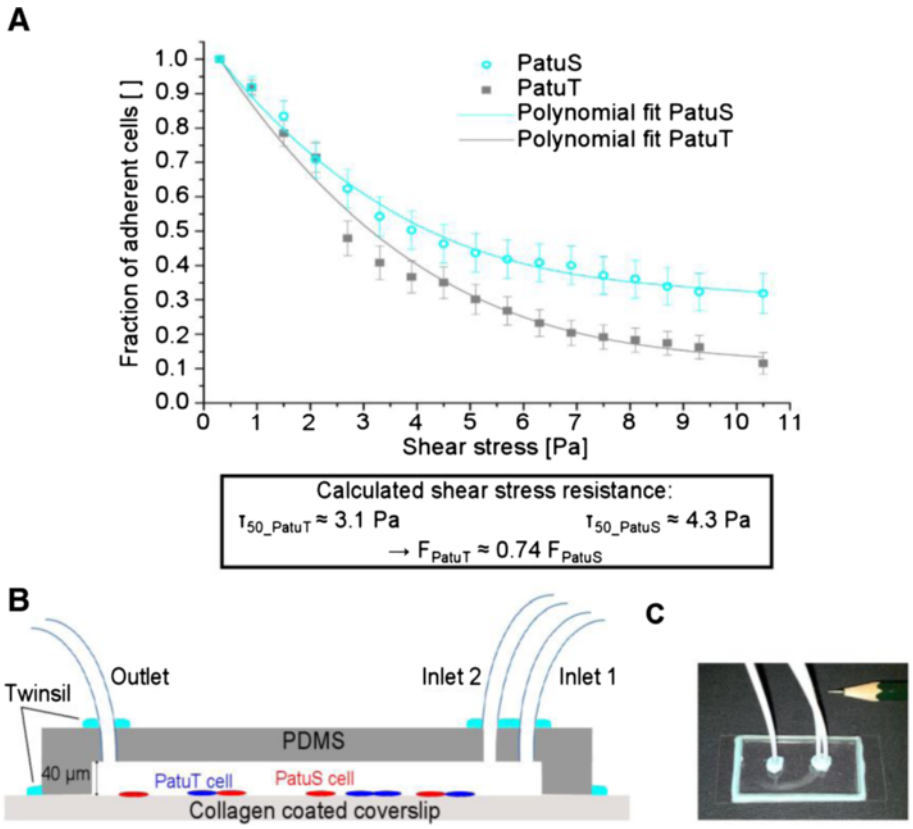


**Figure 2 Microfluidic cell detachment assay and flow chamber. (A)** The detachment assay determines the fraction of adherent cells after exposure to increasing shear stress. PatuT and PatuS cells were allowed to adhere for 90 min before starting up the flow. Error bars represent the SEM. The critical shear stress $\tau_{50}$ where 50% of the cells were detached defines the adhesion strength. A schematic sketch **(B)** and a photograph **(C)** of the flow chamber are shown. The flow cell is mounted on a collagen-coated coverslip. The flow chamber consists of two inlets and one outlet. The cells within the flow cell are fluorescently labeled.

(Applied Precision Inc.) on an Olympus IX inverted microscope (Olympus) using a a 20× magnification objective (0.50 Ph 1 UPlanFl, Olympus). For the detachment assay the channel was flowed with cell culture media (1% serum) and the flow rate increased in a stepwise manner. The initial flow rate was 20 µl/min to remove loosely attached cells. We increased the flow rate in increments of 40 µl/min up to a maximal rate of 700 µl/min. At each step the medium flowed for one minute, then stopped. Images of dye-incorporated cells were recorded employing the respective fluorescence filter one minute after stopping the flow. After each flow step the remaining cells were counted and plotted, after normalization to the cell count, at a flow rate of 20 µl/min ($\tau = 0.3$ Pa).

## Reflection interference contrast microscopy (RICM)

### *2λ-RICM setup*

The RICM setup was implemented on an inverted microscope Olympus IX71 (Olympus) equipped with an antiflex 63× oil immersion objective (NA 1.25, Neofluar-Antiflex; Zeiss). Samples were illuminated by a fiber-coupled Xenon lamp (R 100 W/45C OFR; Osram) that is coupled into the microscope via a cage system composed of a lens, an iris (to minimize stray light), and a dichroic mirror. The RICM reflector cube within the microscope consists of a polarizer, a dichroic mirror and an analyzer. A beam splitter (560DCXR; AHF Analysetechnik) was used to simultaneously record two wavelengths. Orange light was filtered by a bandpass filter (593/40; AHF Analysetechnik) before it was imaged by a 12 bit CCD camera (Orca-R2; Hamamatsu). Green light was imaged by a second 12 bit CCD camera (Orca-R2; Hamamatsu) and subsequently filtered by a bandpass filter (546/10; AHF Analysetechnik). The entire cage system was covered with a custom-built light protection system to ensure a good image quality with high contrast. The microscope itself was enclosed by a heated and air humidified custom-built chamber.

### *Theory*

Image contrast of RICM results from the interference of light that is reflected at several refractive index boundaries. The reflected rays interfere and give rise to an

interference pattern, which allows an estimation of the object's contour (Figure 1). The intensity distribution of the interference pattern for objects in the (x,y) plane at a given wavelength λ can be described by:

$$I\ (h(x,y),\lambda) = I_1 + I_2 + 2\sqrt{I_1 I_2}\ \cos\left(\frac{4\pi n h(x,y)}{\lambda} + \delta\right) \quad (1)$$

$I(h(x,y),\lambda)$ is the intensity in the interferogram at point $(x,y)$ with a height of $h(x,y)$. $I_1$ and $I_2$ are the intensities of the two interfering beams, $n$ is the refractive index of the medium and $\delta$ is the phase shift of the light reflected from the object, which equals $\pi$ if $n_{object} > n_{buffer}$. In the case that the two interfaces are close together the interferogram shows a minimum. When the membrane is further away from the substrate the path difference increases and the corresponding intensity on the interferogram also increases. It is obvious from the cosine in the interference function that the interference pattern repeats periodically every $\Delta h = \lambda/2n$. By adding a second, or accessorily a third, wavelength the ambiguity of about $\lambda/2$ in the interference pattern can be elided through comparison of the interferograms, allowing the calculation of absolute distances [23,24].

#### *RICM experiments*

Cells were seeded in the microscopy chamber and single cells were imaged every 2 min for the first 60 min after substrate contact formation and then every 5 min for the next 7 hours. Since maximal adhesion area and projected cell area was reached after 60 min, in same cases after 70 min, more extensive adhesion behavior analysis was done during the first hour post plating.

### Data analysis of RICM images

Data analysis was performed with the MATLAB software (R2007b, 1994–2011 The MathWorks, Inc.). Based on an algorithm from the cell segmentation toolbox, the analysis was modified for RICM images. Cell segmentation was used to read out different parameters: projected cell area (in pixel), minimum and maximum intensity value (range 0–255), pixel list (x- and y coordinates of each pixel and its associated intensity value), and intensity histogram. The 3D intensity surface plots were calculated using the information of the pixel list. An intensity threshold was determined to define the contact/adhesion area. The threshold intensity $I_{thresh}$ was derived from equation 1 by setting the threshold membrane-to-substrate distance at 40 nm [25-28] for a wavelength of $\lambda_1 = 593\ nm$ or $\lambda_2 = 546\ nm$ and using the minimum and maximum intensities $I_m$ and $I_M$ on each cell image [29]. This is a semi-quantitative method [25,29] which distinguishes between adherent and non-adherent parts of the cell membrane. Adherent parts are defined as less than 40 nm away from the surface and non-adherent parts as further away.

Pixels with intensities $< I_{thresh}$ are identified as tight adhesion zones and are displayed in black. Pixels with higher intensity values $> I_{thresh}$ are displayed in white, creating a binary display of the cell showing the fraction and distribution of contact areas within the cell.

#### *Further image analysis*

The adhesion patches of the threshold images were analyzed with the tool "Analyze particles" in the ImageJ version 1.46a. The spatial distribution of adhesion patches was analyzed with a "radial plot profile" plug-in for ImageJ. The profile plot shows the normalized integrated intensities around concentric circles as a function of distance from a point in the image. From this image point the intensity at any given distance represents the sum of the pixel values around a circle. To yield normalized comparable values the integrated intensity is divided by the number of pixels in the circle that is also part of the image.

### Modeling and mathematical test

All mathematical analyses, including fitting and statistical analysis, were performed with the software OriginPro8.6G (OriginLab, Northampton, MA). In all cases the mean value with its respective standard error is shown.

## Results

### Cell spreading kinetics

In order to precisely identify the starting point of stable adhesion and the differences in the adhesion behavior of the two cell types, we performed live cell imaging directly after cell plating. To identify adhesive areas we used a semi-quantitative analysis [25] to distinguish between adherent and non-adherent areas within the projected cell area. To this end, we applied a threshold intensity corresponding to a cell-to-substrate distance of 40 nm [26]. Figures 3A & B show RICM images and respective threshold images of a representative PatuT and PatuS cell at different stages of cell spreading, namely 16, 30 and 60 min post plating. The threshold images of RICM micrographs illustrate the formation and development of adhesion zones within the cells and show that adhesion patches are distributed differently in the two cell lines. For a more detailed analysis of spreading kinetics the mean projected cell area as well as the mean adhesion area within the first 70 min post plating were plotted for both cell lines (Figure 3C). The projected cell area of the two cell lines differed in dimension and

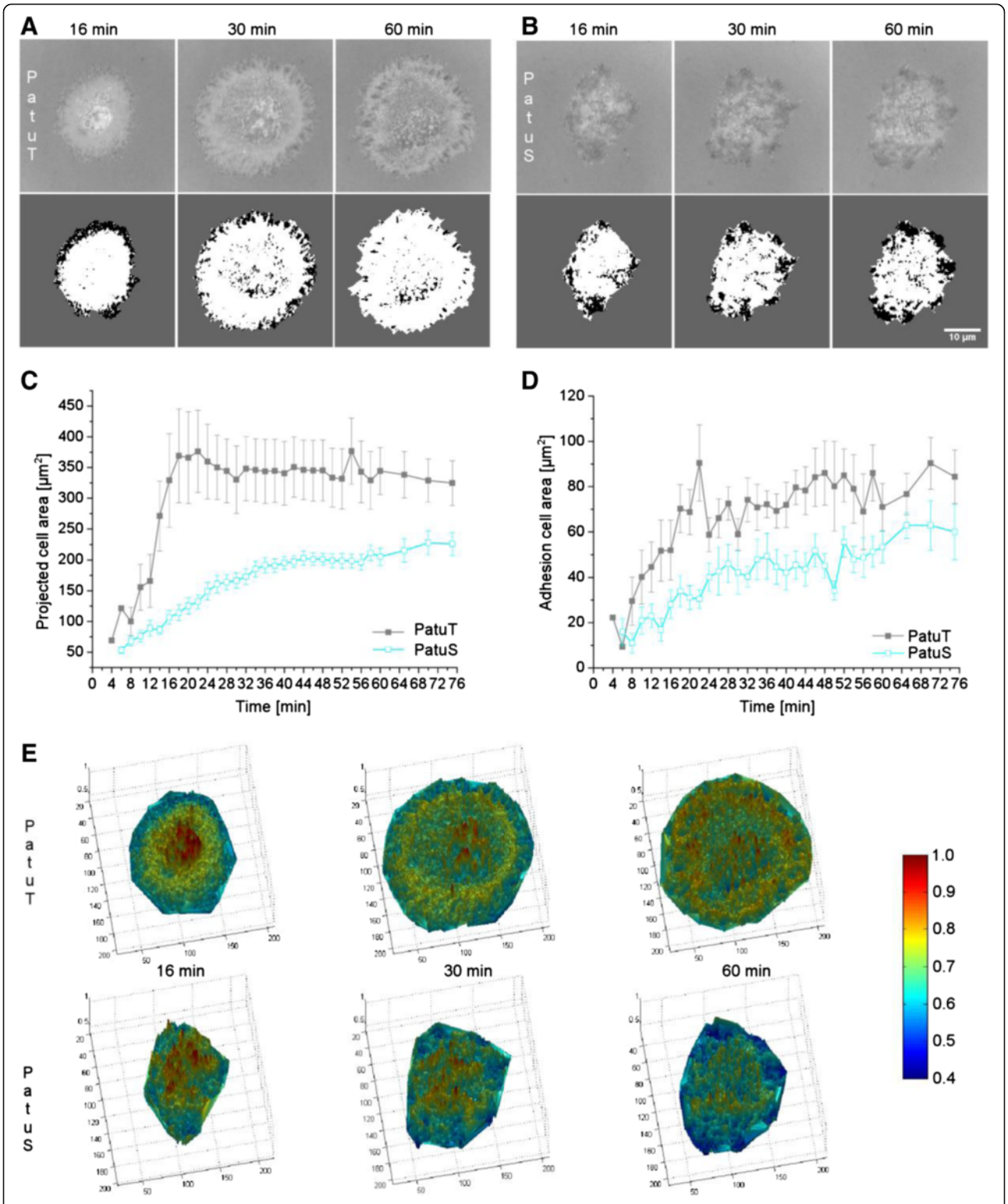


**Figure 3 Cell adhesion kinetics.** RICM images and corresponding threshold images at various stages of cell spreading for PatuT **(A)** and PatuS cells **(B)** at 16, 30, and 60 min post plating (Scale bar: 10 µm). Cell spreading kinetics for the average projected cell area **(C)** and the average adhesion area **(D)** of the two cell lines. Error bars represent the standard errors of the mean (SEM). Characteristic normalized intensity profile plots **(E)** of the interface of a typical PatuT (top) and PatuS (bottom) cell for the same time points are shown. The distances are color-coded from close (blue) to far (red).

formation kinetics. PatuT cells showed a 40% larger projected cell area than PatuS cells. They also reached their maximum projected cell area after about 20 min, which is three times faster than their sister cell line (~ 70 min). The initial growth within the first several minutes was greater and notably faster for PatuT than for PatuS cells. PatuT cells exhibited a projected cell area of approximately 60 $\mu m^2$ at four minutes post plating and doubled their area within two minutes, whereas PatuS cells had a projected cell area of about 50 $\mu m^2$ at six minutes post plating and doubled their area within 10 minutes.

In contrast to the different time course for achieving the maximum projected cell area, maximum adhesion area (as measured by RICM) was reached for both cell lines after approximately the same amount of time (Figure 3D). The final adhesion area of PatuT cells was only ~30% larger than that of PatuS cells. This is remarkable considering the 40% difference in the projected cell area of the two cell lines. In sum, the ratio between adhesion and projected cell area was smaller for the more malignant, dedifferentiated and E-cadherin negative PatuT cells than for the highly differentiated, E-cadherin expressing PatuS cells. This indicates a loss of adhesion capability for the more malignant cell line PatuT. The representative intensity plot profiles of a single cell of each cell line visualize the existence of more pronounced adhesion parts in PatuS than in PatuT cells (Figure 3E). The intensity values obtained from the RICM image were normalized to the highest occurring value in the image. The color gradient from blue to red reflects the cell to substrate distance from close to distant. PatuT cells often exhibited more homogeneously distributed, smaller adhesion zones. Those adhesion zones of PatuS cells that grew during the first 60 min post plating were found to have the shape of larger patches and were localized in the cell periphery.

### Adhesion patch distribution

Since both cell lines showed clear differences in cell spreading and adhesion kinetics, we next specified their adhesion patches. The topography, as seen in the intensity profile plots in Figure 3E, provides detailed insight into the adhesion areas, thus revealing differences between the two analyzed cell lines. Adhesion contacts are defined as areas of closest distance between the membrane and the substrate (see Additional file 1 Figure S1). These findings contradict the work of Iwanaga et al. [30]. For a more detailed study, we next created heat maps of the adhesion pattern (Figure 4A) of each cell and investigated these adhesion patterns with regard to their spatial location (Figure 4B), their number and their size (Figure 4C). The heat maps of the adhesion patterns of two representative cells shown in Figure 4A visually reproduce the differences in the adhesion patch size of the two cell lines. The color code reflects the size of the adhesion patches from green (0–2.42 $\mu m^2$) over blue to red (14.58 - 17.01 $\mu m^2$).

We analyzed the spatial distribution of adhesion patches using ImageJ. To this end, we produced plot profiles of normalized integrated intensities around approximated concentric circles as a function of distance from a specific point in the binary threshold images of the cells. Figure 4B shows the average profiles for both cell lines 16 and 60 min post plating. The intensity of the averaged radial profiles of PatuT cells decreased over time, which illustrates the growth of adhesion zones during this time span. The smaller the integrated intensity the more adhesion zones became apparent within the cell. Furthermore, the adhesion zones in PatuT cells were distributed evenly over the entire cellular contact zone. In contrast, adhesion zones of PatuS cells were distributed inhomogeneously with a clear preference for the cell periphery. This is apparent by the appearance of a clear minimum in the integrated intensity. The minimum turning point in the radial profiles of PatuS cells, which represents the smallest integrated intensity in the curve, also progressed outwards with increasing adhesion time. The smallest integrated intensity is inversely correlated with the amount of adhesion area within the cell. Thus, the adhesion zones obviously grow within the first 60 min, all the while moving outwards. In addition, the normalized integrated intensity was smaller for PatuS cells. This is reflected in a greater number of black pixels in the cell images, indicating more adhesion patches in these cells.

#### *Size distribution of adhesion patches*

To analyze adhesion patches with regard to their number and size, we used the particle analyzer tool in ImageJ. The first time point that was analyzed was 16 min after plating. Here, PatuS cells exhibited more small adhesion patches with a size of 1.7-3.3 $\mu m^2$ than PatuT cells (PatuS: ~35%; PatuT: ~29%) Figure 4C). In contrast, mid-size patches in the size range between 3.4-13.4 $\mu m^2$ were more numerous on PatuT (~62%) than on PatuS cells (~48%). Significantly more patches with a size >13.4 $\mu m^2$ were found on PatuS cells than on PatuT cells (PatuS ~ 17%; PatuT ~ 9%). After 60 min a change in the size distribution occurred: on PatuT cells patches of smaller sizes were now in the majority (not the mid-sized patches, as had been the case after 16 min). After 60 minutes 51% of patches belonged to the small size range, whereas only 32% mid-sized patches and 18% large patches were visible. After 60 min the number of midsized patches continued to decrease, while at the same time the number of small and large patches increased. Patch size distribution in PatuS cells followed a different pattern: patches within the small and medium size range decreased in number with time. This

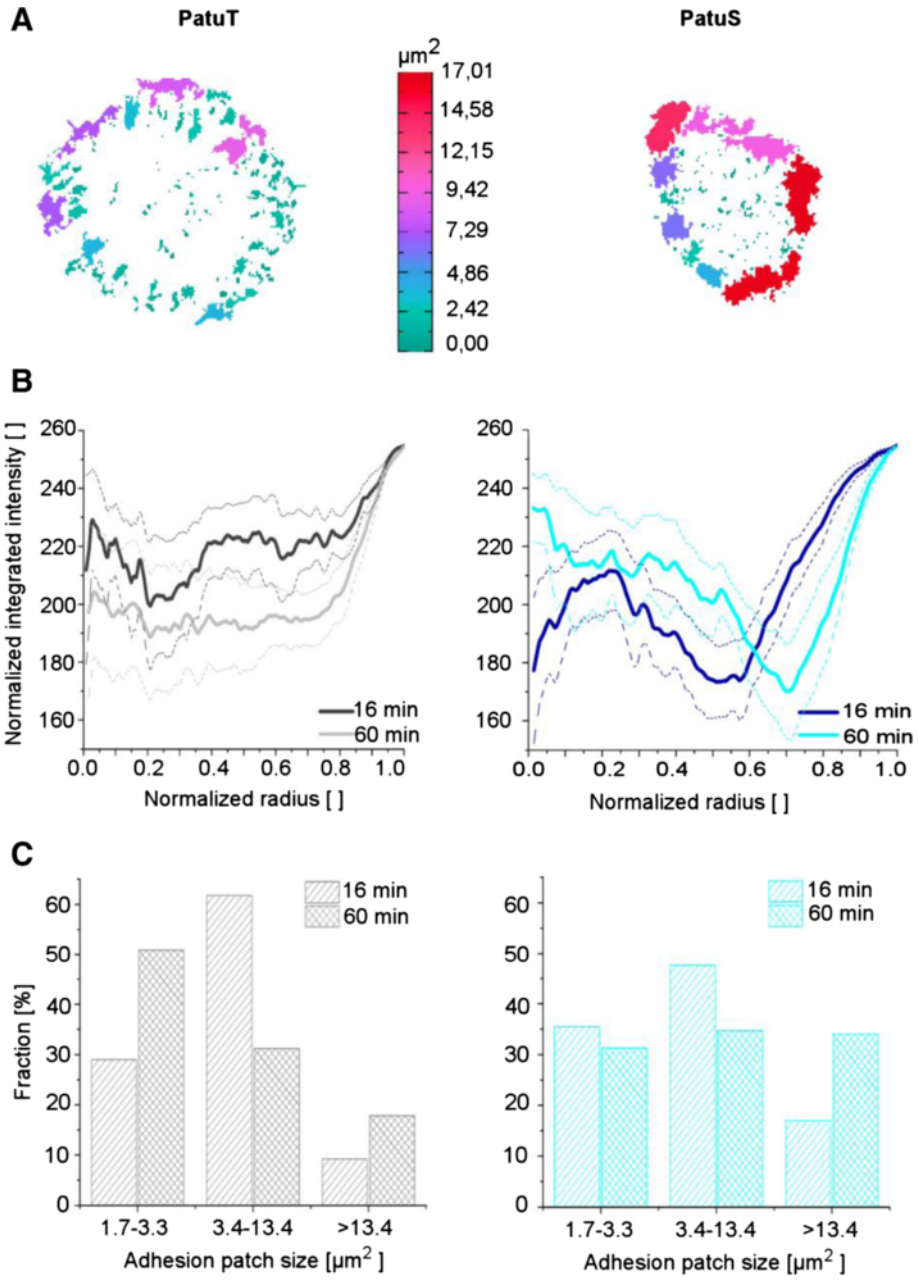


**Figure 4 Adhesion patch analysis.** Heat maps of the adhesion patches for a selected PatuT (left) und PatuS cell (right) 60 min after plating **(A)**. The radial distribution of adhesion patches is shown as the average of the normalized integrated intensity versus the normalized radius for PatuT and PatuS **(B)**. The smaller the integrated intensity the more adhesion zones within the cell pattern become apparent. Dashed lines represent the SEM. The adhesion patch size distributions for both cell lines 16 and 60 min after plating are shown in **(C)**.

coincided with an increase of large patches, resulting in a nearly balanced size distribution (small: ~31%, medium: ~35%, large: ~34%) 60 min after plating.

In sum, based on our observations – namely the lower ratio of adhesion area to projected cell area for PatuT cells, the differences in patch size distributions, and, additionally, the differences in the spatial distribution of adhesion patches between both cell lines – we conclude that the more malignant cell line, PatuT, exerts less adhesion force onto the substrate than the benign cell line, PatuS. To verify this we investigated both cell lines with regard to adhesion strength using a microfluidic detachment assay.

### Cell detachment assay

Cell detachment assays measure the ease with which cells can be detached. In our assay cells were exposed to

a hydrodynamic flow within a flow channel. Cell detachment was achieved by increasing the flow rate in a stepwise manner. The detachment assay was started 90 min after seeding to ensure that cells had formed functional adhesion zones. Based on a Poiseuille model for parallel plate flow channels the generated channel wall shear stress τ, the cause for cell detachment, can be described with equation 2 [31]:

$$\tau = {}^{6}\eta Q/_{(h^2 w)} \quad (2)$$

$\eta$ is the viscosity [kg/ms], $Q$ the flow rate [$m^3$/s] of the liquid, $h$ the height, and $w$ the width of the channel. In Figure 2A the fraction of adherent cells as a function of shear stress is shown. The two most notable findings were: Firstly, the behavior of the two cell lines differed above a specific shear stress threshold ($\tau \approx$ 2.7 Pa). Secondly, above this threshold PatuS displayed a stronger ability to remain adherent. Using this plot we determined the critical shear stress $\tau_{50}$ where 50% of cells were detached and assigned the value $\tau_{50}$ to the mean adhesion strength. PatuT cells were able to withstand a critical shear stress of $\tau_{50,\mathrm{PatuT}} = 3.1$ Pa. In contrast, PatuS cells persevered at a much higher shear stress of $\tau_{50,\mathrm{PatuS}} = 4.3$ Pa. This result shows that the adhesion strength of PatuT cells is only 74% of that of PatuS cells ($F_{\mathrm{PatuT}} = 0.74\ F_{\mathrm{PatuS}}$). This confirms our hypothesis stating that the more malignant PatuT cell line suffers from reduced adhesion strength.

#### Adhesion strength model on the basis of RICM images

Finally, we also rated adhesion strength directly from the RICM images with the help of a mathematical model. The model we applied is based on the model of integrin-mediated cell adhesion strengthening parameters to overall adhesion strength, described in *Gallant et al. (2005)* [32]. Gallant et al. employed this model to calculate the force of single adhesion patches with regard to integrin bond force, bond numbers and bond distribution along the contact area. Using our adaption of this model the adhesion strength of the entire cell can be described with the help of the adhesion maps obtained from RICM images. For this, we divided each cell into different circular zones $i$, which were centered on the cell's middle and differed in their radius. The resultant force $F$ produced by each zone $i$ can then be calculated using the following force rule:

$$F_i = fB_i\left[\varepsilon + (1-\varepsilon)e^{1-i}\right] \quad (3)$$

$f$ is the individual integrin–ligand bond strength, $B_i$ the number of bonds in zone $i$, and $\varepsilon$ the fraction of bonds associated with cytoskeletal focal adhesion (FA) elements (from $\varepsilon$ =0: no FA to $\varepsilon = 1$: all FA). The adhesion strength of the entire cell can then be described by the sum of the strength in each zone:

$$F_{cell} = \sum_i F_i \quad (4)$$

Two stress distributions can be described with equation 3 by modeling the parameter ε: 1) an uniform stress model where the spatial arrangement of the adhesion patches is irrelevant because all bonds break simultaneously, and 2) a peeling model, where the spatial arrangement of the adhesion patches influences the cell adhesion strength. The uniform stress model assumes that all bonds within the contact area are uniformly stressed. It defines cell detachment as the moment when all bonds break simultaneously. From this we can deduce that in this uniform stress model all bonds are associated with focal adhesion elements and that $\varepsilon = 1$. This results in an adhesion force $F_i$ that solely depends on the number of bonds in that specific circular zone and on their individual integrin-ligand bond strength $B_i$ ($F_i = f\ B_i$). The peeling model, on the other hand, describes cell detachment as a peeling-off process. It assumes that bonds on the cell periphery are subject to greater stress than the interior bonds. Detachment in this case resembles the undoing of a clothing zipper. When the force on the periphery exceeds the maximum bond strength, the bond breaks and the boundary layer moves inward, assuming that the bond stress decays exponentially with increasing distance from the cell edge. This process can be modeled with $\varepsilon = 0$, which results in an adhesion force of $F_i = f\,B_i\,e^{1-i}$.

In the following, we present the model on the basis of the RICM results for adhesion at 60 min after cell seeding. Figure 5 depicts the conditions for each cell line as obtained from the cell analysis: PatuT cells show smaller, homogeneously distributed adhesion patches (Figure 5 left), whereas PatuS cells showed fewer and larger adhesion patches which, in addition, were preferentially located in the cell periphery (Figure 5 right).

In the model, PatuS cells were divided into six circular zones, covering their entire projected cell area. In contrast, PatuT cells – which have a larger projected cell area than PatuS cells – were divided into ten circular zones. We used the information obtained from the radial plots to determine adhesion patch positions (Figure 4B). Based on these data, we calculated the percentage of the adhesion area for each of the different circular zones using the normalized cell radius $r$. To perform calculations using equation 3 the use of assumptions is necessary. Concerning the number of adhesion bonds we assumed 26000 bonds and 19500 bonds that are distributed proportionally in all of the circular cell zones for PatuT cells and PatuS cells, respectively. When defining the number

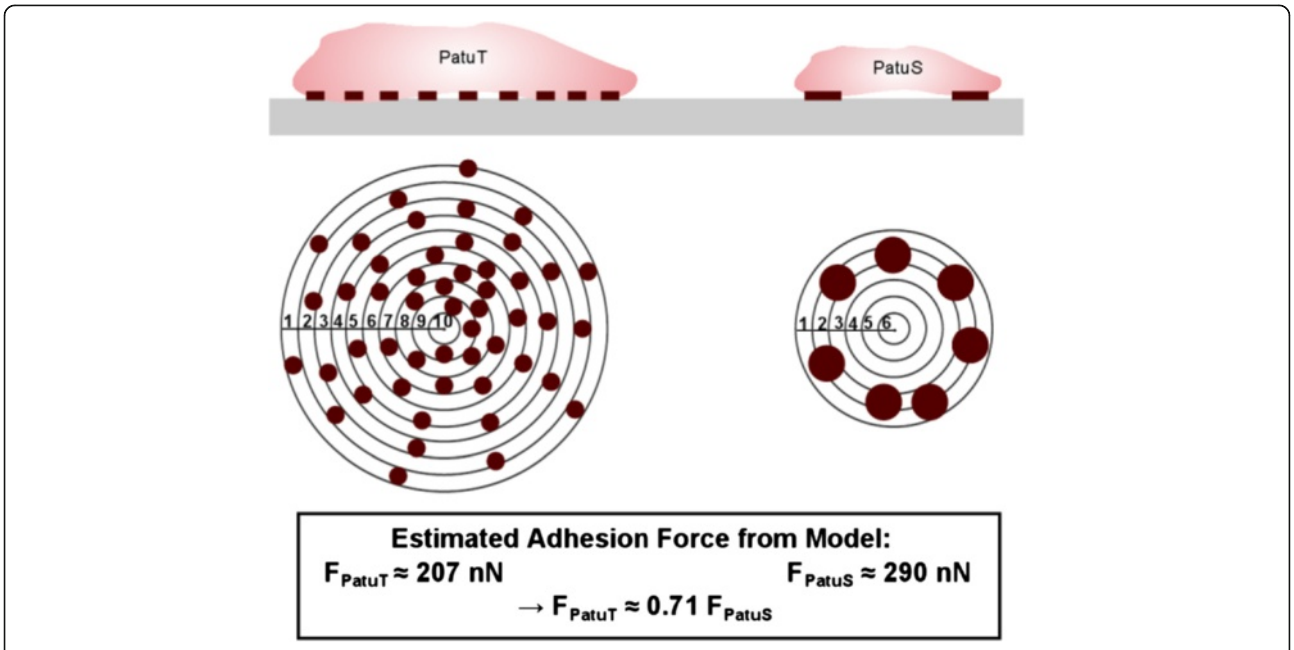


**Figure 5 Adhesion strength model.** Depiction illustrating the parameters of the adhesion strength model. PatuT cells (left) possess numerous small adhesion patches, which are homogeneously distributed over the entire cell contact area. PatuS cells (right) have a 40% smaller projected cell area than PatuT cells and adhesion patches are located in the cell periphery as well as distributed in fewer and larger segments. For the model the cells are divided into circular zones centered on the cell's middle and numbered from the cell periphery to its center. The estimated adhesion force from the model was 207 nN and 290 nN for PatuT and PatuS cells, respectively.

of bonds for each cell line we took the smaller absolute adhesion area of the PatuS cells and the resulting smaller number of bonds into account. We chose the bond numbers based on the following values: the integrin head domain diameter of 9 nm [33] and a distance of approximately 50 nm between integrins in the adhesion patch, which is comparable to the size of intracellular FA proteins like talin [34,35]. Based on these values we calculated the receptor density at $3.7\times10^{10}$ / $cm^2$, which lies within the previously reported density range of $10^7$-$10^{11}$ / $cm^2$ [36].

In a next step, we assigned ε values for calculating forces. For this we factored in the size of the adhesion patches and used simplified assumptions. We also took into consideration that one third of the total adhesion area is occupied by focal adhesions and chose ε values such that the sum of the ε values of the three size ranges equaled 1/3 (see Additional file 1: Figure S1 showing the co-localization images of fluorescently labeled focal adhesion protein paxillin with adhesion patches of RICM images of a PatuT cell on collagen after 24 h).

To this end, we made the following three assumptions:

1. Small adhesion patches are not yet clustered and are not stably anchored to the cytoskeleton (there are no focal adhesions) → detachment occurs exponentially with the distance → $\varepsilon = 0$
2. Middle sized adhesion patches contain FAs → 2/3 of the patch area consists of FAs (and the ratio of FAs to the adhesion area is 1/3) → $\varepsilon = 2/3*1/3 = 2/9$
3. Large patches must consist of more than only FAs, because FAs of this large size do not exist → large patches make up 1/3 of the FA fraction → $\varepsilon = 1/3*1/3 = 1/9$.

The calculated adhesion strength – based on these assumptions and the information on the patch size range distribution for both cell lines (see Figure 4C) – is about 30% less in PatuT cells than in PatuS cells ($F_{PatuT} = 0.71\ F_{PatuS}$). This is in good agreement with our microfluidic cell detachment assay showing that PatuT cells exhibit only 74% of the adhesion strength of PatuS cells.

By approximating the force to break a single integrin as an integrin-ligand bond strength of an integrin α2β1 with collagen type I ($f \approx 50$ pN) [37], we can calculate (from equation 3) an adhesion force of $F_{PatuT} \approx 207$ nN and $F_{PatuS} \approx 290$ nN for PatuT and PatuS cells, respectively.

## Discussion

By comparing cell adhesion kinetics we found that the ratio of the adhesion area to the entire cell area differed between the two cell lines: although PatuS cells had both a smaller projected cell area and a smaller adhesion area than PatuT cells, the ratio between the two was larger

for PatuS cells. It is known that cell-substrate adhesion strength decreases as metastatic capacity increases [38]. This finding suggests that as cells progress in their metastatic capacity they produce fewer focal adhesions (FAs), perhaps resulting in a less adhesion-dependent mode of migration. Since a linear relationship between force and area of FAs exists [39,40], we conclude that the malignant, dedifferentiated cell line (PatuT) exerts less adhesion strength to the substrate than the highly differentiated cell line PatuS. This supports findings by *Albersdörfer et al.* (*1997*), who reported in their model membrane study of giant vesicles and supported membranes that the adhesion energy of tight adhesions is larger than the adhesion energy of less adherent regions [41].

To determine adhesion zones in RICM images of cells we used a semi-quantitative threshold method for data analysis. This method is fairly robust concerning the comparison of sequences of images, because the determination of the threshold intensity remains a valid tool if all intensities in an image are influenced equally (e.g., darker illumination in one experiment) or if all intensities are subjected to a linear transformation (e.g., background subtraction or histogram expansion). For our analysis we define the dark zones in the RICM images as areas of close contact between the cell membrane and the substrate. In other words, we consider these to be tight adhesions. This method lacks the ability to measure absolute distances between the cell and substrate, but produces realistic estimates of the adhesion area. This analysis is supported by the co-localization of fluorescent images of focal adhesions and dark patches in RICM images (Additional file 1: Figure S1). The threshold distance of 40 nm that we applied is in good agreement with current literature. Using tandem scanning confocal image analysis, *Davies et al.* (*1993*) ascertained distances of less than 50 nm throughout the adhesion regions of endothelial cells [26]. Experimental estimates of cell to substrate distances range between 20 to 40 nm, which matches the known length of adhesion receptors [25,27,28]. Furthermore, it has been shown that dark areas in RICM images represent focal adhesions [42] and that they can be described as regions of close contact in transmission electron microscopy images [43]. With their immunostaining experiments on fibroblasts *Riveline et al.* (*2001*) were able to prove that dark patches are, indeed, focal adhesions [17]. *Case et al.* (*2011*) showed in combined TIRF-IRM measurements that the appearance of integrin waves coincides, both temporally and spatially, with propagating regions of IRM intensity decrease [44].

Our separation method made it possible to analyze characteristic adhesion patterns found in RICM images. Our two main findings are that the two cell lines differ in their adhesion patterns and that the ratio of the adhesion area to the entire cell area is greater on PatuS cells than on PatuT cells. We suggest that PatuT cells exhibit lower adhesion forces than PatuS cells. This was confirmed by microfluidic detachment assays. The results of these investigations are in good agreement with traction force studies showing that traction stress in two-dimensional cultures and cell-substrate adhesion strength are decreased as metastatic capacity increases. In addition, a reduction in the overall number of focal adhesions and the level of active beta-1 integrin are indicators of an increased metastatic capacity of the cell [38]. Because there is a linear relationship between the internal forces exerted by a focal adhesion and its lateral size [39], the adhesion strength can potentially be used to estimate the invasiveness of tumor cells. Several published theoretical studies correlate cell adhesion strength only with spread cell area [31,45]. At the same time, the influence of the effective adhesion area is neglected. Here we show that the cell's spread area must not necessarily scale with its adhesion strength, since larger spread PatuT cells generally show less adhesion strength than less spread PatuS cells.

Furthermore, our RICM image-based adhesion strength model shows that the spatial distribution and the size of adhesion patches influence the adhesion strength, proving PatuT cells to have less adhesion strength. By approximating the force necessary for breaking a single integrin α2β1-collagen bond at 50 pN [37] and assuming a receptor density of $3.7\times10^{10}/\mathrm{cm}^2$ (assuming a distance of 50 nm between integrins and an integrin diameter of 9 nm [33]), we obtain an adhesion strength of around 200–300 nN for the two cancer cell lines. AFM studies on non-tumor cells (fibroblasts), for example, found an even greater adhesion strength of 350–580 nN [46,47].

The method we used to quantify cellular adhesion strength does not require an elastic substrate, such as is the case for traction force microscopy or pillar bending assays. Nor does it need the application of external force for pulling the cells off the substrate, which is the case in AFM type experiments. Instead, our method has clear advantages, namely the possibility to measure the distribution and size of adhesion plaques without the use of a marker and the chance to calculate the adhesion force per cell without physically disturbing the cell.

## Conclusion

The aim of the work was to identify and separate cells according to their characteristic adhesion fingerprint, and thereby make it possible to classify the tumor grade. In summary, we could show that RICM is a novel, label-free tool highly suitable for classifying tumor cells. By visualizing the process of contact formation between cells and planar surfaces many characteristic parameters can be read out of the obtained RICM images.

One important parameter for the classification of malignancy is the adhesion strength. Our method, based on RICM image analysis and the calculation of the adhesion strength using the adhesion strength model we developed, is the first time that adhesion patterns extracted from RICM images are used for the direct calculation of adhesion strength. The model we developed includes two different detachment models: the uniform stress model considers the influence of focal adhesions [32], whereas the peeling model describes the force distribution as a function of the position of adhesion patches within the cell [48,49]. By adding further parameters, such as the dynamics of adhesion patches, the accuracy of the malignancy prognosis can be improved.

In future, an adhesion map library of multiple tumor cells, which would allow the comparison of individual parameters, could be generated. Our long-term goal is to establish a computer-aided-diagnostics (CAD) system for biopsy samples, much like those now used in clinics to retrieve conspicuous structures and sections in MRI or x-ray scans. We show that RICM imaging is an easily setup microscopy technique from which multiple adhesion-related parameters can be read out, processed by advanced image analysis and used to categorize tumor cells according to pathology grading systems. Furthermore, the summary of the different applied pattern recognition algorithms on single cell images results in an undistinguishable fingerprint. Our newly developed method has the potential to optimize cancer therapy.

## Additional file

**Additional file 1: Figure S1.** Colocalization images of fluorescently labeled focal adhesion protein paxillin with adhesion patches of RICM images of a PatuT cell on collagen after 24 h. (A) Epifluorescent image of immunocytochemical stained paxillin clusters. (B and C) RICM images of PatuT cells, captured at wavelengths of $\lambda 1 = 593$ nm and $\lambda 2 = 546$ nm. Dark areas represent tight adhesions. Overlay images are shown in (D and E). Scale bar: 10 μm.

#### Abbreviations

ECM: Extracellular matrix; FA: Focal adhesions; PatuT: Patu8988t; PatuS: Patu8988s; RICM: Reflection interference contrast microscopy; SEM: Standard error of the mean.

#### Competing interests

The authors declare that they have no competing interests.

#### Authors' contributions

Conceived and designed the experiments: KK, VCH-W, JPS. Performed the experiments: KK, CER. Analyzed the data: KK, VCH-W, JPS. Wrote the paper: KK, VCH-W, JPS. All authors read and approved the final manuscript.

#### Acknowledgments

We thank Timo Maier and Dr. Tamás Haraszti for the hardware & software installation of the RICM-Setup and Dr. Nina Grunze for very helpful general corrections. Dr. Frank Narz (Qiagen) contributed with many fruitful discussions. The work was part of a BMBF initiative. Part of the research leading to these results has received funding from the European Union Seventh Framework Programme (FP7/2007-2013) under grant agreement n° NMP4-LA-2009-229289 Nano II and n° NMP3-SL-2009-229294 Nano CARD. JPS is the Weston Visiting Professor at the Weizmann Institute of Science. The group is part of the excellence cluster Cell Networks at the University of Heidelberg. The support of the Max Planck Society is highly acknowledged.

#### Author details

[1]Department of New Materials and Biosystems, Max Planck Institute for Intelligent Systems, Stuttgart, Germany, and Department of Biophysical Chemistry, University of Heidelberg, Heidelberg, Germany. [2]Biomedical Technology Center, University of Münster, Münster, Germany.

Received: 20 August 2013 Accepted: 11 October 2013
Published: 28 October 2013

#### References

1. Arcangelis AD, Georges-Labouesse E (2000) Integrin and ecm functions: roles in vertebrate development. Trends Genet 16(9):389–395
2. Danen EHJ, Sonnenberg A (2003) Integrins in regulation of tissue development and function. J Pathol 201(4):632–641. doi:10.1002/path.1472, http://dx.doi.org/10.1002/path.1472
3. Fournier MF, Sauser R, Ambrosi D, Meister JJ, Verkhovsky AB (2010) Force transmission in migrating cells. J Cell Biol 188(2):287–297, doi: 10.1083/jcb.200906139
4. Trappmann B, Gautrot JE, Connelly JT, Strange DGT, Li Y, Oyen ML, Cohen Stuart MA, Boehm H, Li B, Vogel V, Spatz JP, Watt FM, Huck WTS (2012) Extracellular-matrix tethering regulates stem-cell fate. Nat Mater 11(7):642–649, doi: 10.1038/nmat3339
5. Prager-Khoutorsky M, Lichtenstein A, Krishnan R, Rajendran K, Mayo A, Kam Z, Geiger B, Bershadsky AD (2011) Fibroblast polarization is a matrix-rigidity-dependent process controlled by focal adhesion mechanosensing. Nat Cell Biol 13(12):1457–1465, doi: 10.1038/ncb2370
6. Christ KV, Turner KT (2010) Methods to measure the strength of cell adhesion to substrates. J Adhes Sci Technol 24(13–14):2027–2058
7. Jin H, Varner J (2004) Integrins: roles in cancer development and as treatment targets. Br J Cancer 90(3):561–565, doi: 10.1038/sj.bjc.6601576
8. Ke XS, Qu Y, Goldfinger N, Rostad K, Hovland R, Akslen LA, Rotter V, Øyan AM, Kalland KH (2008) Epithelial to mesenchymal transition of a primary prostate cell line with switches of cell adhesion modules but without malignant transformation. PLoS One 3(10):e3368, doi: 10.1371/journal.pone.0003368
9. Mani SA, Guo W, Liao MJ, Eaton EN, Ayyanan A, Zhou AY, Brooks M, Reinhard F, Zhang CC, Shipitsin M, Campbell LL, Polyak K, Brisken C, Yang J, Weinberg RA (2008) The epithelial-mesenchymal transition generates cells with properties of stem cells. Cell 133(4):704–715, doi: 10.1016/j.cell.2008.03.027
10. Woodhouse EC, Chuaqui RF, Liotta LA (1997) General mechanisms of metastasis. Cancer 80(8 Suppl):1529–1537
11. Hategan A, Sengupta K, Kahn S, Sackmann E, Discher DE (2004) Topographical pattern dynamics in passive adhesion of cell membranes. Biophys J 87(5):3547–3560, doi: 10.1529/biophysj.104.041475
12. Curtis ASG (1964) The mechanism of adhesion of cells to glass: a study by interference reflection microscopy. J Cell Biol 20(2):199–215, doi: 10.1083/jcb.20.2.199
13. Gingell D, Todd I (1979) Interference reflection microscopy. a quantitative theory for image interpretation and its application to cell-substratum separation measurement. Biophys J 26(3):507–526
14. Rädler J, Sackmann E (1993) Imaging optical thicknesses and separation distances of phospholipid vesicles at solid surfaces. J Phys II 3:727–748, doi: 10.1051/jp2:1993163
15. Kruss S, Erpenbeck L, Amschler K, Mundinger TA, Boehm H, Helms HJ, Friede T, Andrews RK, Schön MP, Spatz JP (2013) Adhesion maturation of neutrophils on nanoscopically presented platelet glycoprotein Ibα. ACS Nano, DOI: 10.1021/nn403923h
16. Klein K, Maier T, Hirschfeld-Warneken VC, Spatz JP (2013) Marker-free phenotyping of tumor cells by fractal analysis of reflection interference contrast microscopy images. Nano Lett, DOI: 10.1021/nl4030402, in press
17. Riveline D, Zamir E, Balaban NQ, Schwarz US, Ishizaki T, Narumiya S, Kam Z, Geiger B, Bershadsky AD (2001) Focal contacts as mechanosensors: externally applied local mechanical force induces growth of focal contacts by an mdia1-dependent and rock-independent mechanism. J Cell Biol 153 (6):1175–1186

18. Lee J, Jacobson K (1997) The composition and dynamics of cell-substratum adhesions in locomoting fish keratocytes. J Cell Sci 110(Pt 22):2833–2844
19. Elsässer HP, Lehr U, Agricola B, Kern HF (1992) Establishment and characterisation of two cell lines with different grade of differentiation derived from one primary human pancreatic adenocarcinoma. Virchows Arch B Cell Pathol Incl Mol Pathol 61(5):295–306
20. Marques IJ, Weiss FU, Vlecken DH, Nitsche C, Bakkers J, Lagendijk AK, Partecke LI, Heidecke CD, Lerch MM, Bagowski CP (2009) Metastatic behaviour of primary human tumours in a zebrafish xenotransplantation model. BMC Cancer 9:128, doi: 10.1186/1471-2407-9-128
21. Duffy DC, McDonald JC, Schueller OJ, Whitesides GM (1998) Rapid prototyping of microfluidic systems in poly(dimethylsiloxane). Anal Chem 70(23):4974–4984, doi: 10.1021/ac980656z
22. Lohmueller T, Bock E, Spatz JP (2008) Synthesis of quasi-hexagonal ordered arrays of metallic nanoparticles with tuneable particle size. Adv Mater 20(12):2297–2302, doi: 10.1002/adma.200702635
23. Picart C, Sengupta K, Schilling J, Maurstad G, Ladam G, Bausch A, Sackmann E (2004) Microinterferometric study of the structure, interfacial potential, and viscoelastic properties of polyelectrolyte multilayer films on a planar substrate. J Phys Chem B 108(22):7196–7205, doi: 10.1021/jp037971w
24. Schilling J, Sengupta K, Goennenwein S, Bausch AR, Sackmann E (2004) Absolute interfacial distance measurements by dual-wavelength reflection interference contrast microscopy. Phys Rev E Stat Nonlin Soft Matter Phys 69(2 Pt 1):1–021
25. Pierres A, Benoliel A, Bongrand P (2002) Cell fitting to adhesive surfaces: a prerequisite to firm attachment and subsequent events. European Cells and Materials 3:31–45
26. Davies PF, Robotewskyj A, Griem ML (1993) Endothelial cell adhesion in real time. measurements in vitro by tandem scanning confocal image analysis. J Clin Invest 91(6):2640–2652, doi: 10.1172/JCI116503
27. Dustin ML, Cooper JA (2000) The immunological synapse and the actin cytoskeleton: molecular hardware for t cell signaling. Nat Immunol 1(1):23–29, doi: 10.1038/76877
28. Heath J (1982) Adhesions to substratum and locomotory behavior of fibroblastic and epithelial cells in culture. Press VIII + 615, Cambridge University, pp 77–108
29. Limozin L, Sengupta K (2009) Quantitative reflection interference contrast microscopy (ricm) in soft matter and cell adhesion. Chem Phys Chem 10(16):2752–2768, doi: 10.1002/cphc.200900601
30. Iwanaga Y, Braun D, Fromherz P (2001) No correlation of focal contacts and close adhesion by comparing gfp-vinculin and fluorescence interference of dil. Eur Biophys J 30(1):17–26
31. Christophis C, Grunze M, Rosenhahn A (2010) Quantification of the adhesion strength of fibroblast cells on ethylene glycol terminated self-assembled monolayers by a microfluidic shear force assay. Phys Chem Chem Phys 12(17):4498–4504, doi: 10.1039/b924304f
32. Gallant ND, Michael KE, García AJ (2005) Cell adhesion strengthening: contributions of adhesive area, integrin binding, and focal adhesion assembly. Mol Biol Cell 16(9):4329–4340, doi: 10.1091/mbc.E05-02-0170
33. Xiong JP, Stehle T, Diefenbach B, Zhang R, Dunker R, Scott DL, Joachimiak A, Goodman SL, Arnaout MA (2001) Crystal structure of the extracellular segment of integrin alphav beta3. Science 294(5541):339–345, doi: 10.1126/science.1064535
34. Critchley DR (2009) Biochemical and structural properties of the integrin-associated cytoskeletal protein talin. Annu Rev Biophys 38:235–254
35. Kanchanawong P, Shtengel G, Pasapera AM, Ramko EB, Davidson MW, Hess HF, Waterman CM (2010) Nanoscale architecture of integrin-based cell adhesions. Nature 468(7323):580–584, doi: 10.1038/nature09621
36. Cozens-Roberts C, Quinn JA, Lauffenberger DA (1990) Receptor-mediated adhesion phenomena. model studies with the radical-flow detachment assay. Biophys J 58(1):107–125, doi: 10.1016/S0006-3495(90)82357-2
37. Taubenberger A, Cisneros DA, Friedrichs J, Puech PH, Muller DJ, Franz CM (2007) Revealing early steps of alpha2beta1 integrin-mediated adhesion to collagen type i by using single-cell force spectroscopy. Mol Biol Cell 18(5):1634–1644
38. Indra I, Undyala V, Kandow C, Thirumurthi U, Dembo M, Beningo KA (2011) An in vitro correlation of mechanical forces and metastatic capacity. Phys Biol 8(1):015,015, doi: 10.1088/1478-3975/8/1/015015
39. Balaban NQ, Schwarz US, Riveline D, Goichberg P, Tzur G, Sabanay I, Mahalu D, Safran S, Bershadsky A, Addadi L, Geiger B (2001) Force and focal adhesion assembly: a close relationship studied using elastic micropatterned substrates. Nat Cell Biol 3(5):466–472, doi: 10.1038/35074532
40. Schwarz US, Balaban NQ, Riveline D, Bershadsky A, Geiger B, Safran SA (2002) Calculation of forces at focal adhesions from elastic substrate data: the effect of localized force and the need for regularization. Biophys J 83(3):1380–1394, doi: 10.1016/S0006-3495(02)73909-X
41. Albersdörfer TA, Feder SE (1997) Adhesion-induced domain formation by interplay of long-range repulsion and short-range attraction force: a model membrane study. Biophys J 73(1):245–257
42. Abercrombie M, Dunn G (1975) Adhesions of fibroblasts to substratum during contact inhibition observed by interference reflection microscopy. Exp Cell Res 92(1):57–62
43. Chen WT, Singer SJ (1982) Immunoelectron microscopic studies of the sites of cell-substratum and cell-cell contacts in cultured fibroblasts. J Cell Biol 95(1):205–222
44. Case LB, Waterman CM (2011) Adhesive f-actin waves: a novel integrin-mediated adhesion complex coupled to ventral actin polymerization. PLoS ONE 6(11):e26,631
45. Christ KV, Williamson KB, Masters KS, Turner KT (2010) Measurement of single-cell adhesion strength using a microfluidic assay. Biomed Microdevices 12(3):443–455, doi: 10.1007/s10544-010-9401-x
46. Marcotte L, Tabrizian M (2008) Sensing surfaces: challenges in studying the cell adhesion process and the cell adhesion forces on biomaterials. IRBM 29:77–88, doi: 10.1016/j.rbmret.2007.11.019
47. Rahmouni S, Lindner A, Rechenmacher F, Neubauer S, Sobahi TR, Kessler H, Cavalcanti-Adam EA, Spatz JP (2013) Hydrogel micropillars with integrin selective peptidomimetic functionalized nanopatterned tops: a New tool for the measurement of cell traction forces transmitted through αv β3 - or α5 β1 -integrins. Adv Mater, doi: 10.1002/adma.201301338, In press
48. Schmid-Schoenbein GW, Fung YC, Zweifach BW (1975) Vascular endothelium-leukocyte interaction; sticking shear force in venules. Circ Res 36(1):173–184
49. Evans EA (1985) Detailed mechanics of membrane-membrane adhesion and separation. i. continuum of molecular cross-bridges. Biophys J 48(1):175–183

doi:10.1186/1559-4106-8-28
**Cite this article as:** Klein *et al.*: **Cell membrane topology analysis by RICM enables marker-free adhesion strength quantification.** *Biointerphases* 2013 **8**:28.